

1 **Classification:** Biological Sciences/Cell Biology

2

3

4 **Structure of the fission yeast actomyosin ring during constriction**

5 *Matthew T. Swulius<sup>a,b,1</sup>, Lam T. Nguyen<sup>a,b,1</sup>, Mark S. Ladinsky<sup>a</sup>, Davi R. Ortega<sup>a,b</sup>, Samya Aich<sup>c</sup>, Mithilesh*

6 *Mishra<sup>c</sup>, Grant J. Jensen<sup>a,b,2</sup>*

7 <sup>a</sup> *California Institute of Technology, Pasadena, CA 91125*

8 <sup>b</sup> *Howard Hughes Medical Institute*

9 <sup>c</sup> *Tata Institute of Fundamental Research, India*

10 <sup>1</sup> *These authors contributed equally*

11 <sup>2</sup> *To whom correspondence should be addressed: [jensen@caltech.edu](mailto:jensen@caltech.edu), (626) 395 8827*

12

13

14

15

16 **Keywords:** Cell division, cytokinesis, actomyosin ring, cryoEM, cryo FIB mill

17

18 **Abstract**

19 Cell division in many eukaryotes is driven by a ring containing actin and myosin. While much is known  
20 about the main proteins involved, the precise arrangement of actin filaments within the contractile  
21 machinery, and how force is transmitted to the membrane remains unclear. Here we use cryosectioning and  
22 cryo-focused ion beam milling to gain access to cryo-preserved actomyosin rings in *Schizosaccharomyces*  
23 *pombe* for direct three-dimensional imaging by electron cryotomography. Our results show that straight,  
24 overlapping actin filaments, running nearly parallel to each other and to the membrane, form a loose bundle  
25 of approximately 150 nm in diameter that “saddles” the inward-bending membrane at the leading edge of  
26 the division septum. The filaments do not make direct contact with the membrane. Our analysis of the actin  
27 filaments reveals the variability in filament number, nearest-neighbor distances between filaments within  
28 the bundle, their distance from the membrane and angular distribution with respect to the membrane.

29

30 **Significance Statement**

31 Most eukaryotic cells divide using a contractile actomyosin ring, but its structure is unknown. Here we use  
32 new specimen preparation methods and electron cryotomography to image constricting rings directly in 3D,  
33 in a near-native state in the model organism *Schizosaccharomyces pombe*. Our images reveal the  
34 arrangement of individual actin filaments within the contracting actomyosin ring.

35

36 /body

## 37 **Introduction**

38 Cytokinesis, the final step of cell division in eukaryotic cells, is typically driven by a contractile  
39 actomyosin ring (AMR) primarily composed of actin (1) and myosin (2). Our understanding of the  
40 molecular mechanisms of cytokinesis is most detailed in the rod-shaped unicellular eukaryote  
41 *Schizosaccharomyces pombe* (otherwise known as fission yeast), which shares a remarkably conserved set  
42 of cytokinesis genes with metazoans (3). In *S. pombe*, the AMR undergoes multiple phases known as  
43 assembly, maturation, constriction and disassembly (4), with open questions in each of these four stages.  
44 Due to a lack of information about the precise arrangement of filamentous actin (F-actin) within the force-  
45 generating network of the AMR, we chose to focus on imaging the AMR during constriction.

46

47 In *S. pombe*, glancing sections through plastic-embedded, dividing cells gave the first glimpse of actin  
48 filaments running parallel to the division plane at the front of the septum (5). Unfortunately, the study  
49 yielded limited examples and lacked three-dimensional (3D) information for a full analysis. In an ambitious  
50 pioneering effort, Kamasaki et al., produced 3D reconstructions of entire *S. pombe* AMRs by imaging serial  
51 sections through permeabilized cells decorated with Myosin-S1 fragments (6). The amount of F-actin and  
52 the size of the rings appeared significantly altered by the procedure used for preserving them (details in  
53 discussion), but the continuous bundles that were reconstructed were composed of mixed polarity filaments  
54 running circumferentially around the cell.

55

56 Here we sought to visualize the precise arrangement of F-actin within the AMR and its interface with the  
57 membrane by imaging intact cells in a cryo-preserved state using electron cryotomography (ECT) (7).  
58 Because whole *S. pombe* cells are too thick for ECT, which is limited to specimens thinner than a few  
59 hundred nanometers, we overcame this obstacle by first rapid-freezing dividing cells and then either  
60 cryosectioning them or using the recently-developed method cryo-focused ion beam (FIB) milling to

61 produce thin sections or lamellae suitable for ECT analysis. In this study, ~200-nm wide bundles of  
62 straight, overlapping F-actin were seen “saddling” the septum, but no direct contact between filaments and  
63 the membrane were observed over 3  $\mu\text{m}$  of total AMR circumference. 3D segmentations of the filaments  
64 and membrane allowed for quantitative analysis of the average filament length and number per ring, their  
65 persistence length, nearest neighbor distances between filaments as well as between filaments and the  
66 membrane. Additionally, the angular distribution of filaments and spatial distribution of filament ends were  
67 analyzed. Due to the novelty of the methods and three-dimensional nature of data presented, we urge the  
68 reader to first watch [Movie S1](#) for a visual summary of both the methods and main results.

69

70

## 71 **Results**

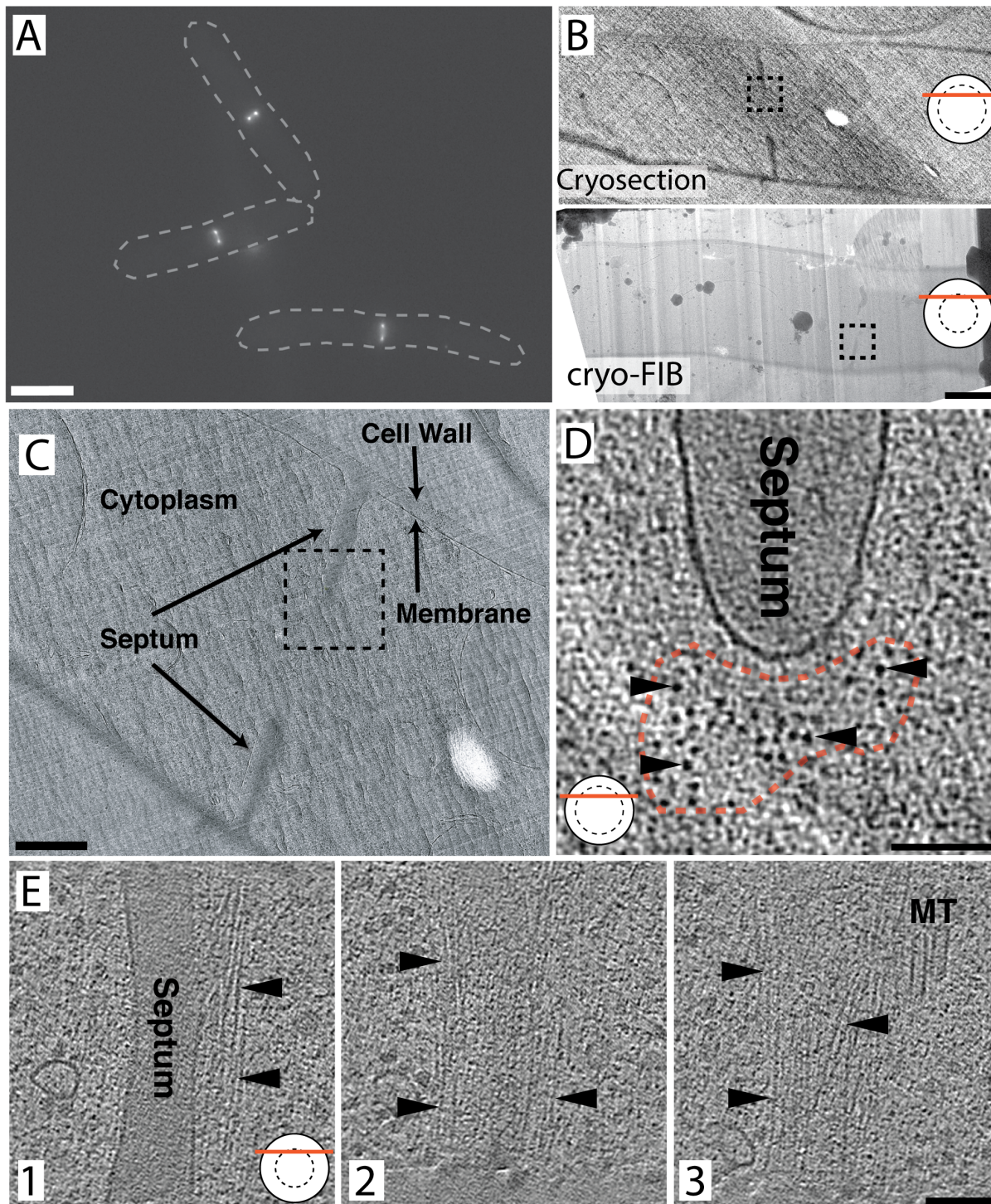
### 72 **ECT of *S. pombe* division sites**

73 To enrich for cells undergoing cytokinesis, we synchronized cells of a temperature sensitive mutant of *S.*  
74 *pombe* (*cdc25-22 rlc1-3GFP*) expressing a GFP-tagged regulatory light chain of myosin (Rlc1-3GFP).  
75 Transient inactivation of the mitotic inducer phosphatase Cdc25p is a commonly employed approach for  
76 synchronization (6, 8, 9), and a detailed characterization of this mutant can be found in the supplementary  
77 information ([Fig. S1 and Experimental Methods](#)). The use of *cdc25-22 rlc1-3GFP* allowed us to monitor  
78 the formation of fluorescent cytokinesis nodes and their coalescence into a continuous fluorescent ring near  
79 the middle of each cell’s length. Once a majority of the rings had begun to contract ([Fig. 1A; Movie S1 at](#)  
80 [0:18](#)), cells were vitrified and thinned by either cryosectioning or cryo-FIB milling. Cryosections ([top of](#)  
81 [Fig. 1B, Movie S1 at 0:46](#)) and cryo-FIB milled lamellae ([bottom of Fig. 1B; Movie S1 at 1:15](#)) were  
82 inspected in a cryo-transmission electron microscope (TEM), and division sites with a visible septum were  
83 targeted for tilt-series collection and tomographic reconstruction ([Fig. 1B–E; Movie S1 at 1:50](#)).

84

85 In total, ~80 tomograms of division sites were generated, and filamentous structures were distinguishable at  
86 the leading edge of the division septum in all of them. Sections cut or milled, simply called sections from  
87 now on, through the division plane nearer to the central region of the ring produced transverse cross-  
88 sections of the contractile ring with putative actin filaments running at small angles with respect to the  
89 electron beam. From this perspective, a cluster of densities (or spots) was identifiable near the front edge of  
90 the septum (Fig. 1D; Fig. 2A–B; SI Appendix/Fig. S2) in tomographic slices (slices of the 3D  
91 reconstruction). Scrolling up and down along the Z-axis of these tomograms revealed that these spots were  
92 cross-sections through filaments that typically traversed the thickness of the entire section, though some of  
93 them terminate within the section (see Movie S1 at 2:29 and red dots in Movie S2 or Fig. 4B). Note that  
94 while small dense spots corresponding to globular proteins were also seen throughout the cytoplasm, they  
95 were not continuous across multiple slices. In seven cases, more tangential sections through a region near  
96 the top or bottom of the ring were reconstructed in which filaments running perpendicular to the electron  
97 beam were visible (Fig. 1E, panels 1–3). As in the transverse sections, filaments in the tangential sections  
98 also lined up in a bundle at the leading edge of the division septum (Fig. 1D–E). Note, however, that except  
99 for the example in Fig. 1E, all tangential sections captured only portions of the bundle making a thorough  
100 analysis from this view implausible.

101



102

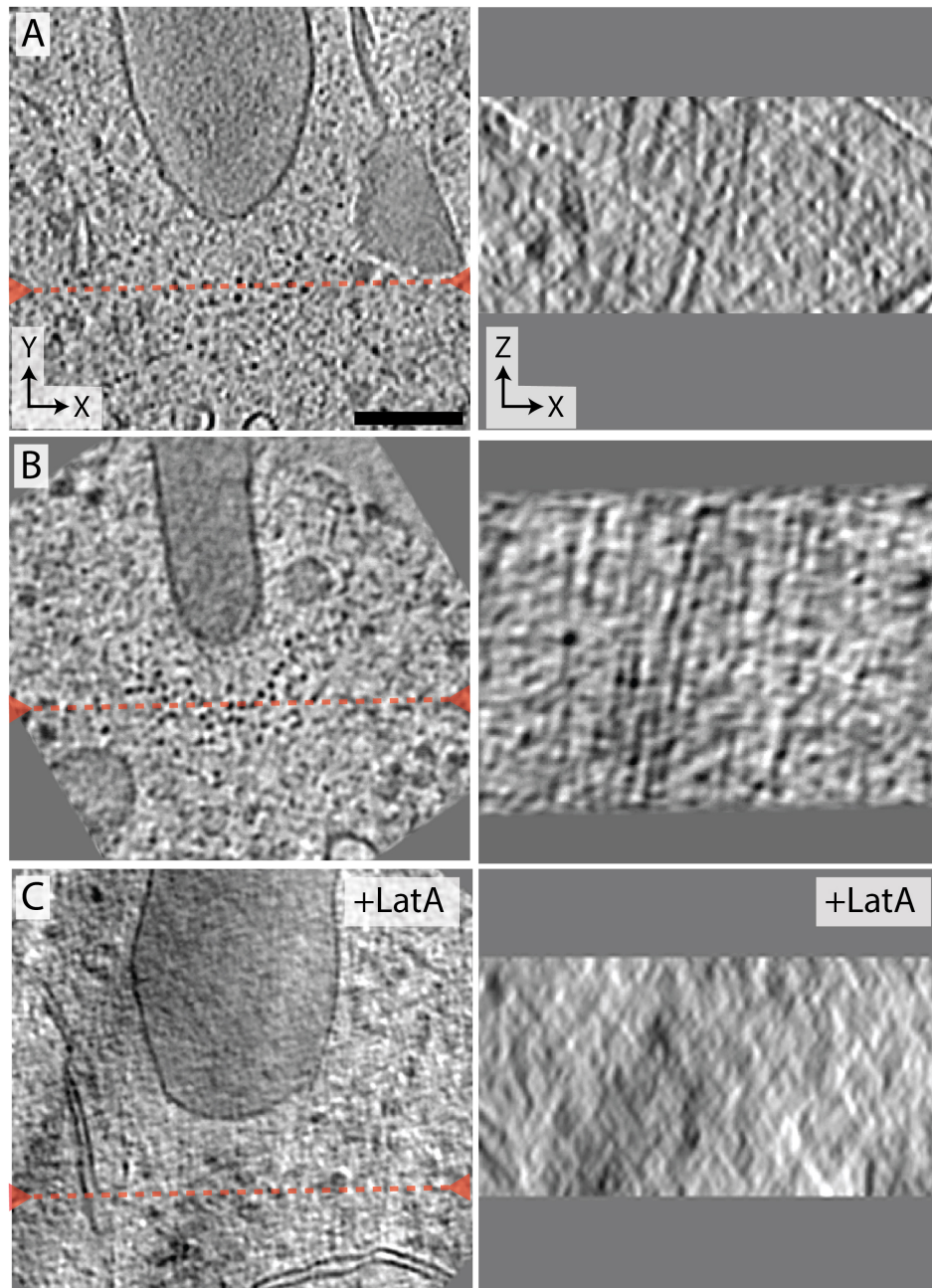
103 **Figure 1:** Imaging the AMR by ECT. (A) Fluorescence image of synchronized, contracting AMRs. Dashed lines indicate  
104 outlines of whole cells for reference. (B) Projection images of a vitreous cryosection (top) and a cryo-FIB milled lamella  
105 (bottom). The boxed region in the top and bottom panel indicate the location of the tomogram in (D) and (E), respectively. (C)  
106 Higher mag projection image of the cryosection through a dividing cell in panel B. The boxed region indicates the location of the  
107 tomogram in (D). (D) Tomographic slice from a transverse cryosection through the AMR, as indicated by the graphic in the  
108 bottom left corner (the solid circle represents the cell in cross-section, the dashed circle represents the ring, and the red line

109 represents the plane of the section through the cell). The red dashed line marks the cross-sectional shape of the actin bundle and  
110 arrowheads point to cross-sections through individual actin filaments. (E) Tomographic slices from a FIB-milled lamella cutting  
111 through the upper portion of the AMR. Slice 1 shows the leading edge of the septum and slices 2 and 3 are progressively further  
112 toward the cytoplasm. Arrowheads point to actin. Two sections of microtubules (MT) are visible. Scale bars represent 5 mm in  
113 panel (A), 1 mm in (B), 500 nm in (C) and 100 nm in (D) and (E). Tomographic slices are 20 nm thick.

114

### 115 **Filaments visualized in the bundle are primarily F-Actin**

116 The molecular identity of each filamentous density within the bundles cannot be easily determined from  
117 visual inspection, but from an ultrastructural perspective they appeared to be composed primarily of F-  
118 actin. In addition to being filamentous (extending through the depth of the tomogram), they were ~7.5-nm  
119 wide, which is consistent with the known size of F-actin. To test this hypothesis, we used ECT on  
120 synchronized dividing cells treated with 10  $\mu$ M Latrunculin A (LatA), which prevents actin polymerization  
121 and led to the loss of F-actin in *S. pombe* within 10 min ([SI Appendix/Fig S3](#)). In all 6 tomograms collected  
122 from LatA-treated cells no filaments were seen at the leading edge of division septa ([Fig. 2C & SI](#)  
123 [Appendix/Fig. S4](#)), further supporting that filamentous densities were F-actin.



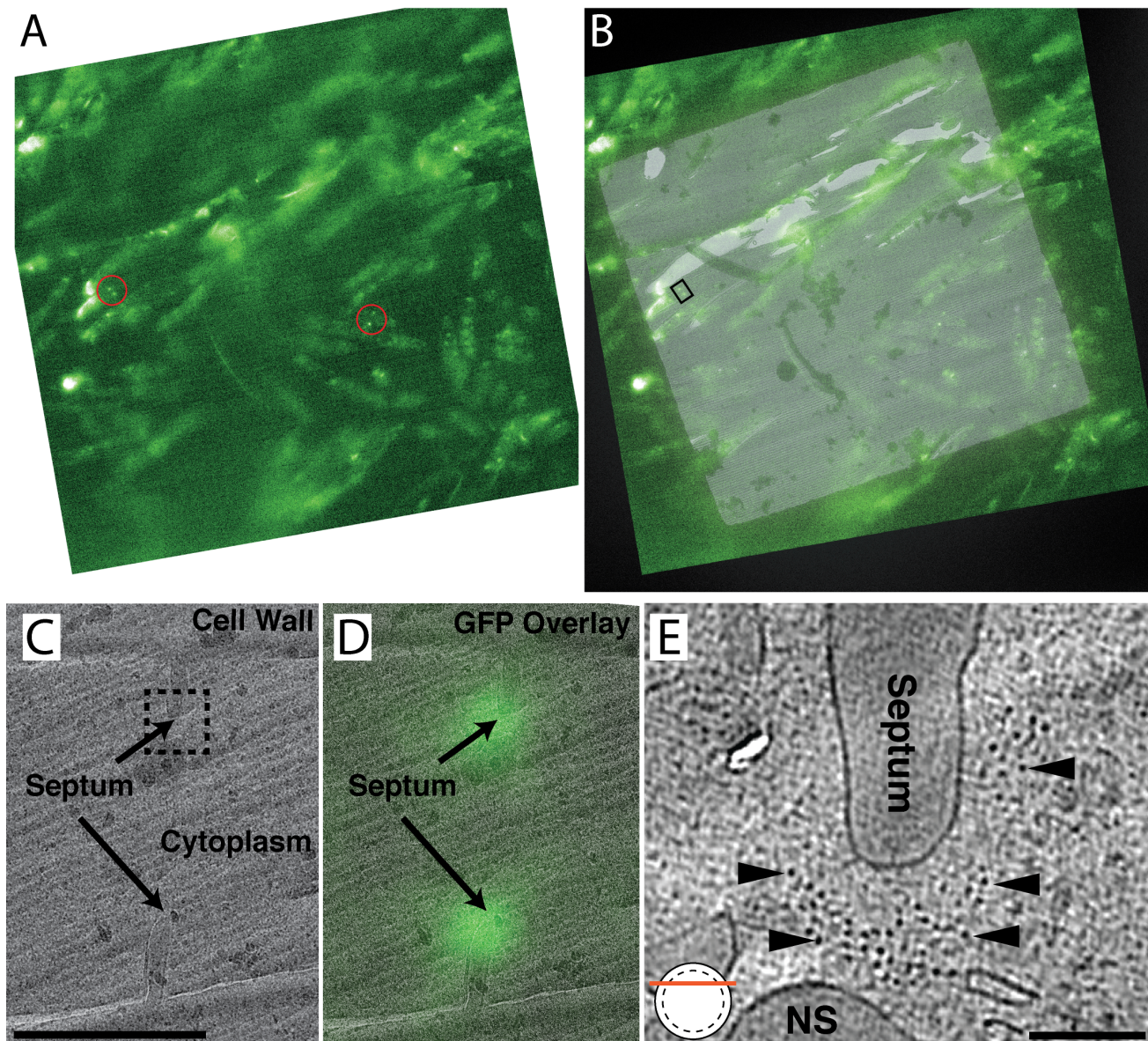
124

125 **Figure 2:** Representative 20 nm-thick slices within transverse sections. The XY slices (left) are perpendicular to the electron  
126 beam and the XZ slices (right) are parallel to the beam at the location indicated by the red dashed line. In (A) and (B) where the  
127 XY slices show a collection of dots near the leading edge of the septum, the corresponding XZ slices reveal streak patterns  
128 indicating the dots are cross-sections of filaments. In (C) where the cells were treated with LatA, the collection of dots and streak  
129 pattern are not seen in the XY and XZ slices, respectively. Scale bar represents 100 nm.

130

131 We were surprised that no obvious myosin motors could be distinguished by eye in our cryotomograms,  
132 and performed correlative light and electron cryomicroscopy (cryoCLEM) on cryosections through

133 dividing *S. pombe* to ensure its presence in the tomograms (Fig. 3; Movie S1 at 3:02). Using the same GFP-  
134 tagged regulatory light chain of myosin II (Rlc1-3GFP), all septa seen in the cryosections (five total), by  
135 fluorescence cryomicroscopy, correlated with bright GFP puncta (Fig. 3A & D), suggesting that myosin II  
136 is present in all of our sections through the AMR. Additionally, tomograms collected on these septa  
137 appeared identical to all of our previous tomograms with only F-actin filaments obviously visible (Fig. 3E).



138  
139 **Figure 3:** Correlated light and electron microscopy of cryosections of dividing *cdc25-22 rlc1-GFP* cells. (A) A single cryo-  
140 fluorescence light microscopy (cryo-FLM) image from a focal stack through one EM grid square that is covered by a vitrified  
141 section of a high-pressure frozen pellet of synchronized dividing cells. Red circles highlight two pairs of sharp fluorescent puncta  
142 indicative of cross-sections through the myosin-containing contractile ring. (B) Overlay of the fluorescent image and a low-  
143 magnification cryoEM image of the cryosection. (C) Higher-magnification image of the region indicated by the small box in

144 panel B, where a division plane is clearly visible. The boxed region indicates the location of the tomogram in panel E. (D) GFP  
145 overlay showing the fluorescent puncta are at the leading edge of the septum. (E) Tomographic slice from a transverse  
146 cryosection through the AMR, as indicated by the graphic in the bottom left. The red dashed line marks the cross-sectional shape  
147 of the actin bundle. Some non-septal (NS) material, which appeared identical to the cell wall in density and texture, is seen in the  
148 cytoplasm. Scale bar represents 1  $\mu$ m in panel C and 100 nm in panel E. The tomographic slice in E is 20 nm thick.

149

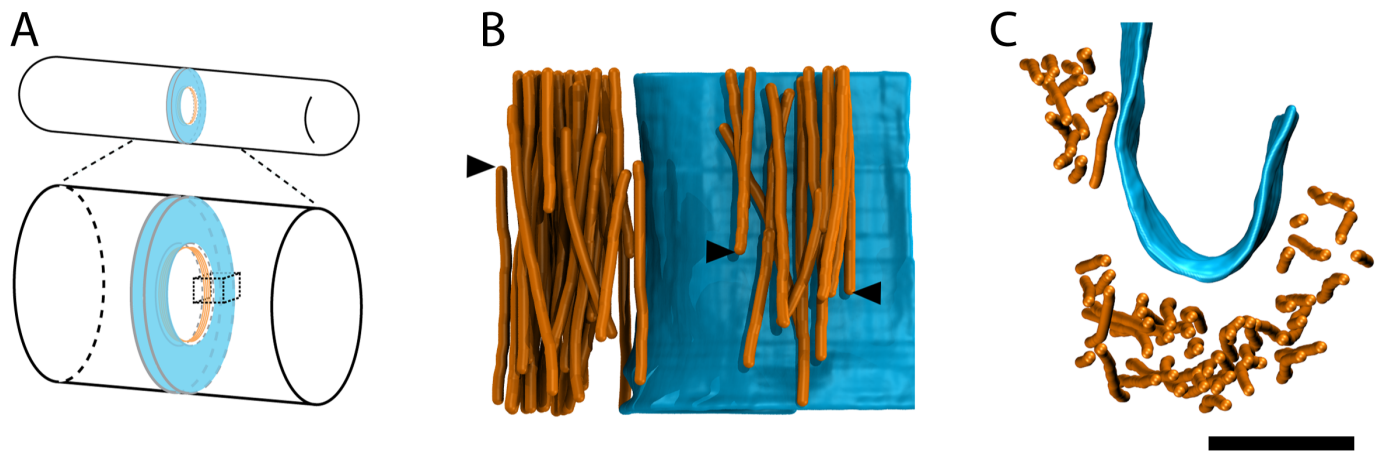
## 150 **Analysis of the F-actin Bundle**

### 151 General Characteristics

152 To analyze AMR filament bundles and their relationship to the membrane, 22 near-to-transverse sections  
153 through the AMR (as in Fig. 3E) were segmented as shown in Figure 4. The plasma membranes were  
154 segmented by hand, while the central line of each actin filament was segmented computationally using an  
155 actin-segmentation algorithm within the Amira software package (10). Using these 3D segmentations, we  
156 counted the number of filaments in each tomogram. On average there were 34 (SD = 12) filaments per  
157 bundle cross-section with individual numbers ranging between 14 and 60 filaments (Fig. 5), which was  
158 largely compatible with quantitative fluorescence microscopy that estimated there would be ~50 filaments  
159 per ring cross-section (11). The majority of filaments traversed the entire thickness of the tomographic  
160 section, but many filament ends were visible as well (arrowheads in Fig. 4B; Movies S2 and S4). From  
161 these 3D segmentations, it was obvious that the cross-sectional boundary of the filament bundle and the  
162 distribution of filaments within the bundle varied (Fig. 5). A few tomograms from different sections  
163 through the same cell were generated (five pairs marked by asterisks in Fig. 5). While the numbers of  
164 filaments were the same in one pair (Fig. 5 O & P), they differed in one pair (Fig. 5 H & I) by a single  
165 filament (30 vs. 29), and the other three pairs (Fig. 5 A & B; L & M; U & V) differed more substantially  
166 (20 vs. 29; 29 vs. 35; 55 vs. 42). Top-views of the 3D segmentations also revealed variance in the cross-  
167 sectional shape of the filament bundle in all five of these cases. Further, filament bundles were pleomorphic  
168 and individual filaments did not adhere to rigid lateral constraints like those observed in the sarcomere of  
169 muscle (12). In nearly half the cases (10 of 22), the filaments within the bundle cross-section could be

170 divided into “sub-bundles” (SI Appendix/Fig. S6; Movie S3) separated by gaps at least 22 nm wide, which  
171 is too far apart to be connected by either the fission yeast actin crosslinker  $\alpha$ -actinin or fimbrin (we  
172 estimated the length of *S. pombe*  $\alpha$ -actinin to be 22 nm by combining the length of two actin-binding  
173 domains (5 nm each) and two spectrin repeats (6 nm each) estimated from the PDB structure 4D1E). It’s  
174 probable that these sub-bundles are actually cross-linked to the AMR in the regions of the ring above or  
175 below our ~200-nm thick sections, and it’s also possible that other longer actin-crosslinkers connect these  
176 sub-bundles.

177



178

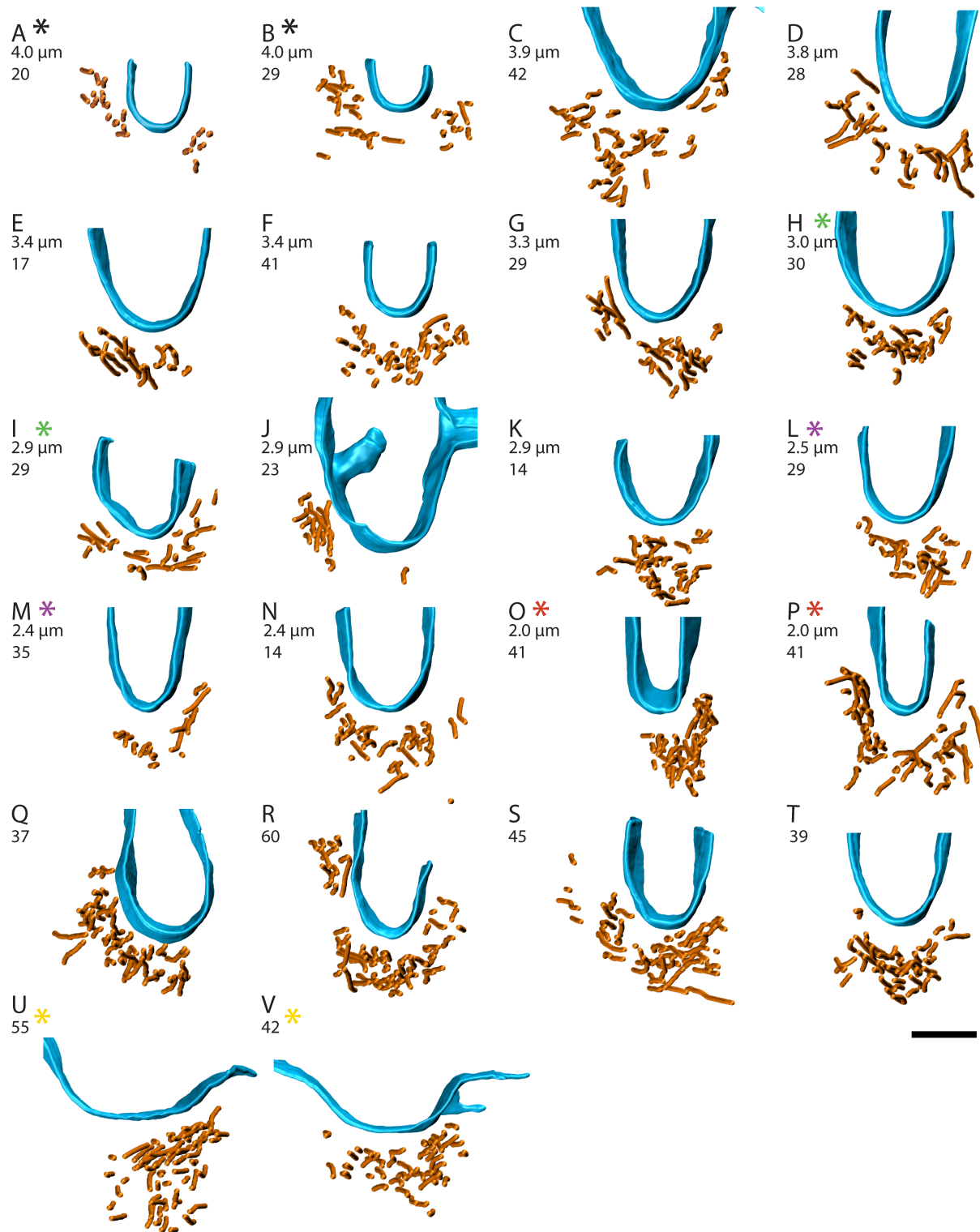
179 **Figure 4:** 3D segmentations of tomographic reconstructions. (A) Schematic of *S. pombe* division septum (blue) and the AMR  
180 (orange) at the leading edge. The dashed cube indicates the portion of the septum represented by the 3D segmentations in panels  
181 B and C. (B) Side view of segmented tomographic reconstruction of actin filaments (orange) and the membrane (blue) from a  
182 transverse section through the AMR. Arrowheads point to filaments that terminate within the section. (C) Top view of the same  
183 segmentation as in panel B. Scale bar represents 100 nm.

184

### 185 Estimating Filament Length and Number

186 Based on the number of filament ends and the thickness of the tomographic sections we estimated that the  
187 average length of the filaments was 910 nm (SD = 550 nm) and on average there were 285 filaments in the  
188 ring (SD = 180). Note that this calculation depends on the assumption that the protein distribution is  
189 uniform around the ring and therefore the filament bundle in each section was representative of the ring.

190 Next, we calculated the ring diameter to determine how these factors depend on the stage of constriction,  
191 but as the ring diameter varied we did not see a clear trend in either the average filament length nor the total  
192 number of filaments in the ring (Fig. 6A & B). The ring diameter calculation could not be done for six  
193 segmented tomograms (Fig. 5 Q–V) due to a lack of corresponding low-magnification images.



194

195 **Figure 5:** Top views of 3D segmentations. The filaments are in orange and membrane in blue. (A–V) show 22 top views  
196 generated from tomographic reconstructions of transverse sections through the AMR, which illustrate the variability in filament  
197 number, variability in cross-sectional shape of the AMR, and correlation between membrane curvature and shape of the  
198 plasmalemmal face of the AMR. The calculated diameter of the ring is shown just below the panel letters (panels A–P) and the

199 other number (A–V) indicates the number of filaments. Color-coded asterisks represent pairs of reconstructions from the same  
200 cell, but from different tomographic sections. Each image corresponds to the same dataset shown in Figure S3. Scale bar  
201 represents 100 nm.

202

### 203 Bundles are Composed of Straight, Nearly Parallel F-actin

204 From visual inspection of the F-actin bundles in three dimensions (see top and side views in [Fig. 5](#) and [SI](#)  
205 [Appendix/Fig. S5](#)) it appeared that all bundles were composed mainly of straight filaments running nearly  
206 parallel to one another. This was quantitatively verified by calculating the straightness of each actin  
207 filament as the ratio of its end-to-end distance to its contour length (see schematic in [SI Appendix/Fig.](#)  
208 [S8A](#)), which revealed a narrow distribution of values between 0.97 and 1 ([Fig. 6C](#)). Alternatively, a  
209 persistence length of  $\sim 5 \mu\text{m}$  was calculated from the tomographic data ([Fig. 6D](#)), which is half that of free  
210 F-actin at  $\sim 10 \mu\text{m}$  ([13](#)), but more than large enough to appear straight in the  $\sim 200\text{-nm}$  thick sections  
211 produced for this study.

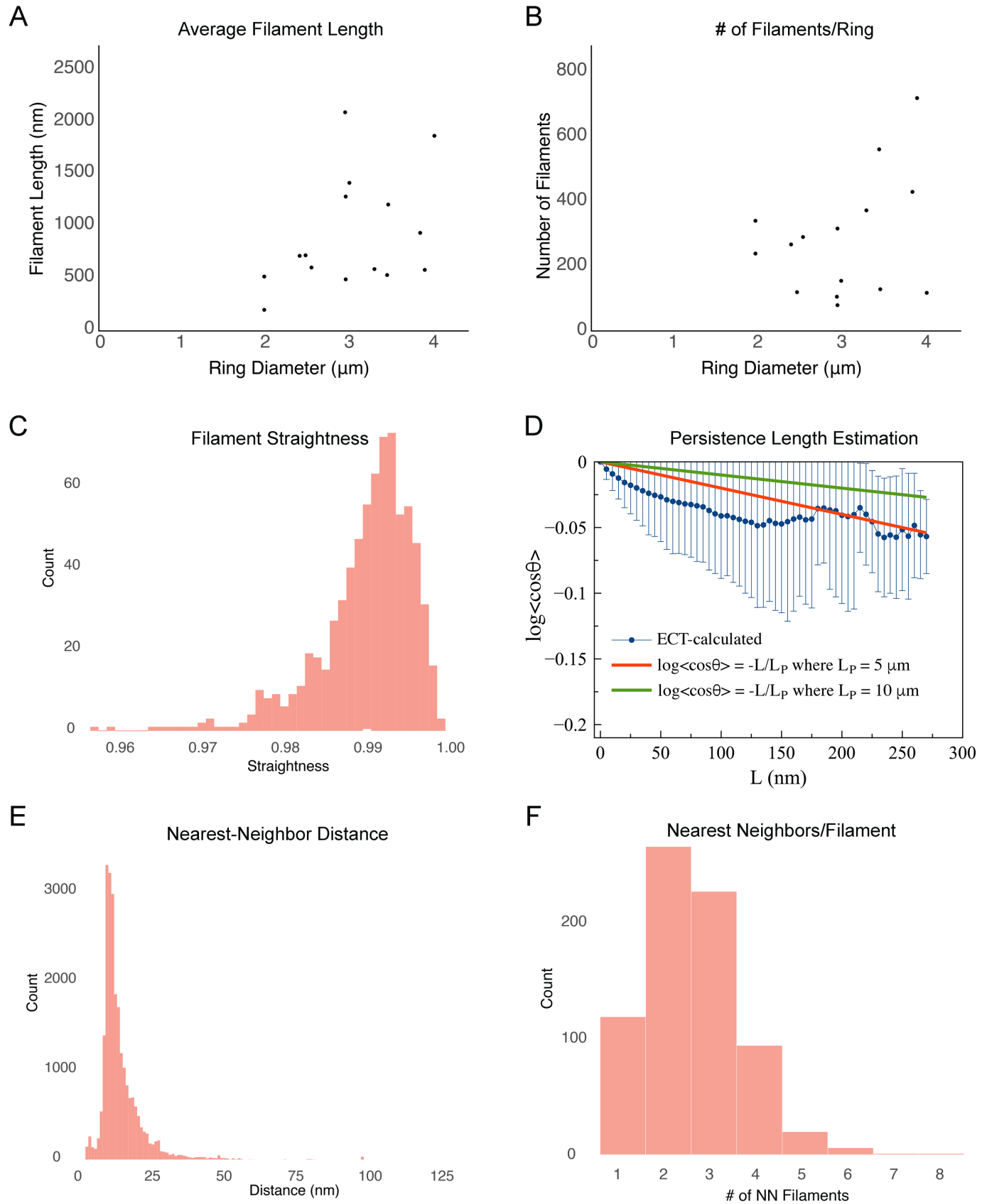
212

213 Next, by representing each filament as a chain of beads, we calculated the distances between all the beads  
214 in the bundle except for those pairs that are part of the same filament. The nearest neighbor distance was  
215 then determined for every bead along every filament, and the combined data from all 22 tomograms  
216 produced a peak that came on sharply at 12 nm and fell off more gradually out to  $\sim 50 \text{ nm}$  ([Fig. 6E](#)),  
217 suggesting that most filaments are cross-linked within the bundle. Our analysis was based on center-to-  
218 center measurements between filaments, which means that the sharp drop-off below 12 nm translates into a  
219 minimum distance of only 4.5 nm between two 7.5 nm-thick filaments. Note that these measurements are in  
220 large agreement with an estimate of  $\sim 15 \text{ nm}$  based on quantitative fluorescence microscopy ([11](#)).

221

222 Finally, in a perfectly parallel bundle of continuous filaments, the nearest neighbor filament should remain  
223 the same throughout a filament's length. However, when we calculated and plotted the number of distinct  
224 nearest neighbor filament-partners for each individual F-actin, we found that individual filaments often had

225 multiple nearest neighbor partners along their length, with a range between 1 and 6, and a peak at 2 (Fig.  
226 6F). This indicates that while the filaments are nearly parallel, there is some degree of intercalation among  
227 them.  
228



229

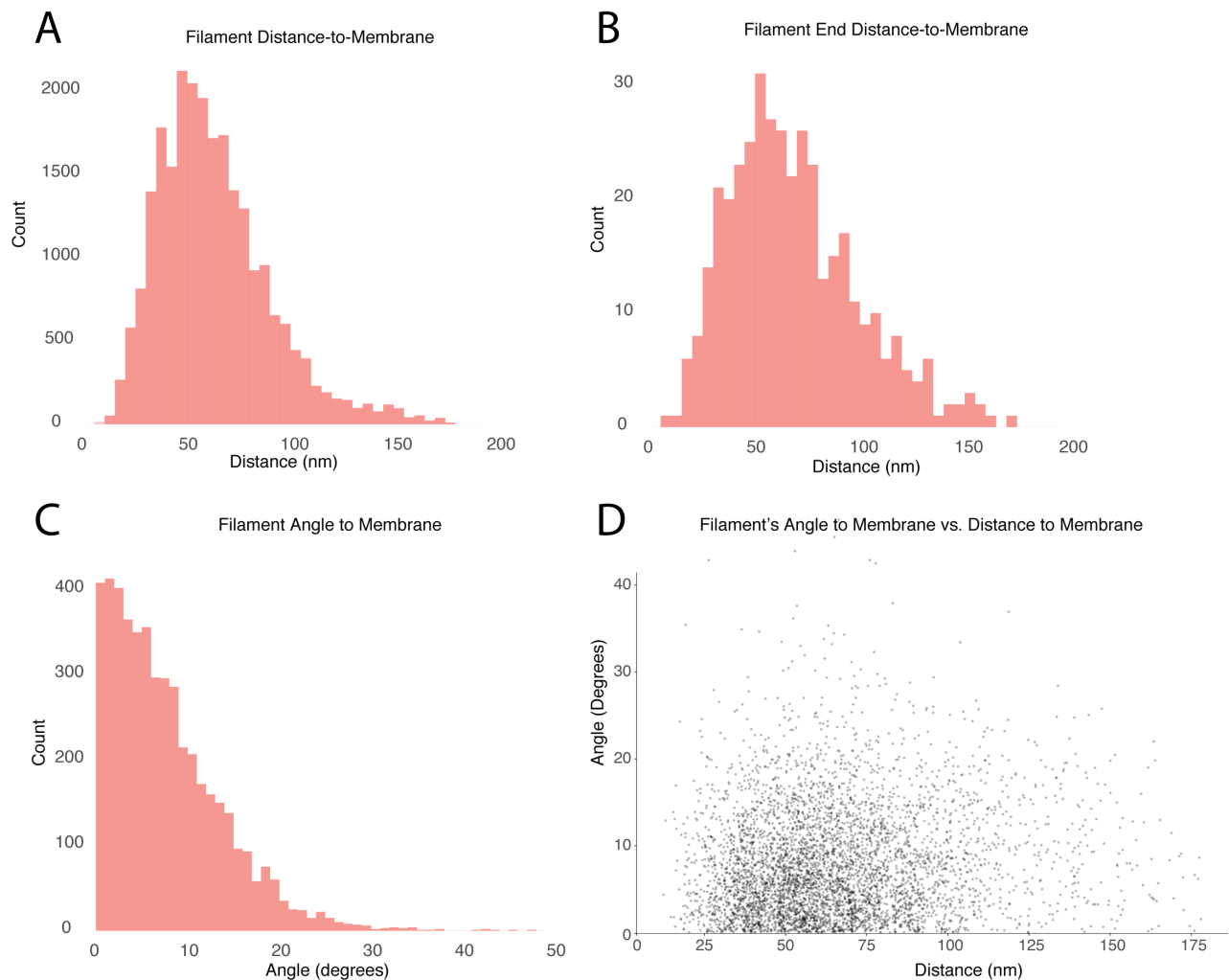
230 **Figure 6:** Quantitative analysis of contractile ring filaments. (A) Scatter plot of the estimated filament length as a function of  
231 ring diameter. (B) Scatter plot of the estimated number of filaments per ring as a function of ring diameter. (C) Histogram of

232 filament straightness, defined as the ratio of the end-to-end distance to the contour length of the filament (see **Methods** for  
233 details). (D) Plot of the persistence length of actin filaments in the tomograms (blue points) compared to the plotted formulas for  
234 persistence length equal to 5  $\mu\text{m}$  and 10  $\mu\text{m}$  (the known value for free actin in solution). Error bars indicate standard deviation.  
235 (E) Histogram of nearest neighbor distances between the filaments. Each filament was modeled as a chain of beads. Pairs of  
236 beads on the same filaments were excluded from the calculation. (F) Histogram of the number of nearest-neighbor partners for  
237 each filament in the tomograms. Except for panels A and B, data were combined from all 22 segmented tomograms (740 total  
238 filaments). The bin size is 0.1 in (C), and 1 nm in (E).

239

## 240 **The Bundle's Relationship to the Membrane**

241 The interface between the bundle and the membrane is of particular importance, because force from the  
242 ring's generated tension needs to be transmitted to the ingressing membrane. To better understand this  
243 interface, we quantitatively characterized the spatial relationship between the filament bundle and the  
244 membrane. First, we calculated the distance between filaments and the membrane by dividing each  
245 filament into 20-nm segments and calculating the distance from the midpoint of each segment to the  
246 membrane (see schematic in [SI Appendix/Fig. S8B](#)). The combined histogram of all 22 tomograms shows a  
247 broad peak between 10 and 150 nm, with a mean value of  $\sim 60$  nm ([Fig. 7A](#)), which produces a bundle size  
248 (100-200 nm across) that agrees largely with the dimensions observed by Kanbe et al in 1989 and by super-  
249 resolution fluorescence ([14](#)). Plotting similar histograms for each tomogram reveals the variability in the  
250 distribution of filaments with respect to the membrane ([SI Appendix/Fig. S7](#)). When the same distance  
251 measurements were made between only the F-actin termini and the membrane, a similar distribution of  
252 distances was observed (11 nm to 177 nm with a median of 66 nm; [Fig. 7B](#)), suggesting that their spatial  
253 distributions are determined by the same factors regulating the distance of the filaments as a whole.



254

255 **Figure 7:** Quantitative analysis of contractile ring filaments with respect to the membrane surface. (A) Histogram of distances  
256 measured from the 20-nm segments ( $N = 5032$ ) of 740 filaments to the membrane. (B) Histogram of the distance measured  
257 between filament-ends and the membrane. (C) Histogram of angles between the 20-nm segments and the membrane. (D)  
258 Scatterplot of the measured distance from the membrane as a function of the segment's angle with respect to the membrane  
259 surface. The bin size is 1 nm in (A) and (B), and 1 degree in (C).

260

261 It appeared by visual inspection of the segmented AMR sections (see top and side views in [Fig. 5](#) and [SI](#)  
262 [Appendix/Fig. S5](#)) that the filaments run nearly parallel to the membrane, and this was verified by  
263 calculating the angle between the membrane and each 20-nm long segment of the filaments (see [SI](#)  
264 [Appendix/Fig. S8B](#)). When the combined measurements from all 22 tomograms were plotted as a  
265 histogram ([Fig. 6C](#)) it showed that nearly all filaments make small angles, with the peak at  $2^\circ$ , and an  
266 average of  $7.8^\circ$  across a range from  $0^\circ$  to  $\sim 50^\circ$ , with the majority falling below  $20^\circ$ . It is not clear what

267 governs the angle of the filaments, but to test whether it was a function of the filament's distance from the  
268 membrane, we plotted the angle vs distance and it revealed no correlation (Fig. 7D).

269

## 270 The Gap

271 There is an obvious gap between the filament bundle and the membrane, but it was difficult with our  
272 current data to make out any regular structures within this region, regardless of the defocus of the specific  
273 tomogram or the thickness of the virtual slice used to view the data. Denoising the tomograms by non-  
274 linear anisotropic diffusion (NAD) filtering did not help reveal any regular, interpretable structures within  
275 the gap either. Occasionally, a thin density extending from the membrane could be seen, but was either  
276 difficult to distinguish from noise or it was rare and unlikely to be responsible for linking the ring to the  
277 membrane. The gap did not contain any visible ribosomes, while many were easily seen elsewhere in the  
278 cytoplasm, suggesting they are specifically excluded or blocked via steric hindrance from the F-actin or  
279 other molecules occupying the gap.

280

281 Despite the lack of visible connections to the membrane, the actin bundle's consistent proximity to the  
282 leading edge of the septum, combined with the way it "saddled" the ingressing membrane, implied a  
283 physical connection must exist between them (Fig. 5 SI Appendix/Fig. S2; Movie S1 at 4:30). The fact that  
284 proteins connecting the actin bundle to the membrane were not visible in the gap suggests an inherent  
285 heterogeneity in the architecture of these connections, and that the connections may have been too thin to  
286 resolve by our method.

287

288

## 289 **Discussion**

290 Here we have presented the first pictures of cryo-preserved AMRs, obtained by ECT of cryosectioned or  
291 cryo-FIB-milled *S. pombe* cells. General dimensions of the ring, measured by ECT, were in agreement with

292 previous EM data from plastic sections of *S. pombe* (5), and from fluorescence imaging (11, 14). However,  
293 the direct imaging of cryo-preserved cells and the three-dimensional nature of electron cryotomography  
294 lead to a more detailed understanding of how individual actin filaments are arranged within the ring and  
295 their spatial relationship to the membrane.

296

### 297 **Comparison with previous thin-section EM studies**

298 We were surprised by how different the results were from those reported in the previous EM study of  
299 spheroplasted, permeabilized, and serially-sectioned cells (6). Apparently, the harsh treatments in the  
300 previous study failed to preserve even gross AMR dimensions, since the *pre-constriction* rings were  
301 reported to be  $\sim 2.5$   $\mu\text{m}$  in diameter, which is only about half of the  $\sim 4.5$   $\mu\text{m}$  one would expect from the  
302 diameter of fission yeast. Furthermore, rings from spheroplasted and permeabilized cells were both 10  
303 times wider along the cell's long axis (based on the thickness and number of serial sections used for  
304 reconstruction) and 2–3 times thicker (based on the scale bar shown) (6). The number of filaments in the  
305 ring seen here and the previous study also differed significantly: 14–60 filaments per cross-section in  
306 vitrified cells versus  $\sim 60$ –180 in the plastic sections (our estimate based on the total number of filaments  
307 reported, their average length, and the ring diameter) (6). It is difficult to know, with certainty, why such  
308 large discrepancies exist, but given the treatment needed to decorate intracellular F-actin with myosin S1  
309 fragments (cell wall digestion and detergent-permeabilization), it is plausible that the AMRs are no longer  
310 under tension because turgor pressure is lost, or that the structure was altered when other binding proteins  
311 (especially myosin) were competed away by the myosin S1 fragments. Additionally, membrane  
312 permeabilization was conducted in the presence of the actin stabilizing molecule phalloidin, which is  
313 known to promote actin polymerization (15) and could account for the increased amount of F-actin in the  
314 serial-sectioned rings.

315

316 Comparing our ECT results with ultrastructural data from sections of plastic-embedded animal cells (16-  
317 18), they share a variety of structural similarities, such as the alignment of filaments parallel to the division  
318 plane. In terms of ring dimensions, the ~200-nm thickness of AMRs in animal cells (16, 17) is largely  
319 compatible with the thickness measured in our ECT data from fission yeast. As expected, however, the  
320 width of the AMR in animal cells is commensurate with its much larger division furrow, which results in  
321 AMRs that are many microns in width (16, 17). In the cleavage furrow of sea urchin eggs the ring was  
322 described as a uniform band of circumferentially-aligned filaments (16), however, multiple small bundles  
323 of actin were observed in HeLa cells (17). These differences might represent natural variation in AMR  
324 architecture across cell types or perhaps reflect different preparation methods, but it is possible that the  
325 single bundle seen here in yeast by ECT represents some basic unit for cell contractility. To this point, the  
326 dimensions of the individual bundles described in HeLa cells (~150 nm in diameter) and their average  
327 number of filaments in cross-section (25 filaments) (17) reasonably fit our ECT data of AMRs in *S. pombe*  
328 (~100 to 200-nm thickness with 34 filaments on average). Short 13-nm wide filaments, presumed to be  
329 myofilaments, were described in HeLa cell AMR bundles, however, and no such myofilament was seen in  
330 our tomograms.

331  
332 While there is a remarkable conservation in the cytokinetic genes of *S. pombe* and animal cells (19), and  
333 some of the differences in ring dimensions between fission yeast and animal cells are simply due to  
334 differences in cell size, there are also fundamental differences in the way rings assemble and function in *S.*  
335 *pombe* compared to animal cells. For instance, *S. pombe* have a cell wall that provides cell rigidity and  
336 shape in the presence of high turgor pressure. There is evidence that cell wall growth in fission yeast  
337 actively contributes to constriction force, and is required to generate forces large enough to counter the  
338 outward force of turgor pressure (20). Animal cells, in contrast, depend on internal cytoskeletal  
339 reinforcement to maintain shape (21), and also have a branched actin cortex linked to the cytoplasmic face  
340 of the plasma membrane, unlike yeast. Currently, evidence suggests that AMRs in animal cells are formed

341 from remodeling this cortical actin, which is already present at, and linked to, the membrane (18, 22).  
342 Direct 3D imaging by ECT in a range of cell types will be required to compare the properties and intrinsic  
343 variability of AMR structures in different systems.

344

#### 345 **The structure of myosin II in *S. pombe* actomyosin ring**

346 Our current ECT data was not able to resolve the structure of myosin motors in the AMR, but correlative  
347 fluorescence data (Fig. 3) showed that myosin was present in our tomograms, suggesting that neither  
348 myosin II isoform in *S. pombe* (Myo2p or My2p) forms the 30-nm thick myofilaments known to exist in  
349 muscle sarcomeres (23). This is a simple logical deduction from the fact that such myofilaments were  
350 readily distinguishable in transverse cryosections through vitrified muscle in previous studies (24). The  
351 structure of purified Myo2p and Myp2p have not been studied by electron microscopy, but myosin II  
352 purified from *Acanthamoeba* self-assembles into a range of oligomeric states, with different thicknesses,  
353 through tail-to-tail interactions (25, 26). If myosin II in *S. pombe* does not form a thick myofilament, it  
354 might adopt one of the other *in vitro* structures observed, such as a simple unipolar or bipolar structure  
355 (made of one or two myosin dimers, respectively), or the intermediate-sized 7-nm thick “minifilament”,  
356 composed of 16 myosins (25, 26). The 7-nm thickness is consistent with the 7.5-nm thick filaments seen in  
357 the AMR, meaning a subset of the filaments seen could be myosin minifilaments. We currently favor the  
358 interpretation that all the filaments we saw were F-actin, however, because no clusters of myosin heads,  
359 like those observed *in vitro* (25, 26), were seen. It is possible, however, that such details were obscured by  
360 the relatively close packing of filaments in the bundle.

361

#### 362 **Crosslinking in the bundle**

363 Even though we could not confidently identify the physical connections between filaments in the bundle,  
364 the relatively tight packing of the filaments suggests that actin crosslinkers were present. Nearest neighbor  
365 distance analysis resulted in a peak at 12 nm, corresponding to a gap of 4.5 nm between the 7.5 nm-thick

366 filaments. This distance is much shorter than both fimbrin and  $\alpha$ -actinin, two known actin crosslinkers that  
367 are present in the ring (27), but it's possible that some unknown crosslinkers of  $\sim 4.5$  nm length may also  
368 be present in the ring. It's also possible that the tension between filaments, generated by myosin, pulled the  
369 filaments as close as they could be to one another, given the flexibility of longer actin cross-linkers like  $\alpha$ -  
370 actinin and fimbrin.

371

## 372 **Connecting the AMR to the membrane**

373 A major question that still remains is how the AMR transfers contractile force to the membrane during  
374 constriction? Our tomograms revealed a clear gap between the bundle and the membrane with no obvious  
375 connecting densities between the actin filaments and the membrane. Additionally, over 3  $\mu\text{m}$  of cumulative  
376 AMR length, no actin filaments made direct contact with the membrane. That being said, it seems highly  
377 likely that there is some physical connection between the bundle and the membrane or it would not stay  
378 localized to the tip of the ingressing septum, nor would its cross-sectional shape saddle the curved edge of  
379 the septum with such consistency, as in our observations.

380

381 The most obvious potential contact points between the ring and membrane are the cytokinetic nodes that  
382 function to recruit and move the major components of the AMR to the division plane during assembly (14,  
383 28-30). These nodes are membrane bound and they contain Myo2p, which interacts with F-actin directly.  
384 They have been shown to persist within the ring during constriction by super-resolution live cell  
385 fluorescence (14). There are  $\sim 140$  nodes per cell, so even assuming the largest diameter ring in our  
386 experiments (4.0  $\mu\text{m}$ ) there would still be one node every 90 nm of AMR on average. That means we  
387 would have captured 1-3 nodes per tomogram (100-300 nm thick). If nodes concentrate as the cell  
388 constricts then we would have captured even more in our tomograms.

389

390 In 2016, Laplante et al. proposed a model of the average cytokinetic node based on both the stoichiometry  
391 and spatial arrangement of proteins within the node measured by super-resolution live-cell fluorescence  
392 (14). Their model node included four Mid1p dimers, four Cdc12p dimers, 8 Rng2 dimers, 8 Cdc15p dimers  
393 and eight Myo2p dimers connected to the node “core” by their coiled-coil tails. The node core (excluding  
394 the thin, flexible Myo2p molecules radiating from it) would be ~5.2 megadaltons with an estimated size of  
395 ~50 nm x 50 nm x 50 nm, which is more massive but significantly larger than the 80S ribosomes (3.2  
396 megadaltons and ~30 nm x 20 nm x 20 nm) that are clearly visible in the cytoplasmic regions of the  
397 tomograms. Presuming the dimensions of the cytokinetic model node is accurate, the 80S ribosome is ~ 5-  
398 fold denser than the cytokinetic node (0.27 kDa/nm<sup>3</sup> vs. 0.05 kDa/nm<sup>3</sup>, respectively), which could account  
399 for why such a large complex was undetectable.

400

401 The average distance between the filaments and the membrane in our cryotomograms (~60 nm), is  
402 consistent with the dimensions of the model node presented by Laplante et al. (14), and their presence  
403 could account for the gap we see between the F-actin bundle and the membrane. It could be that during  
404 constriction the nodes became so densely packed that individual node assemblies could not be  
405 distinguished in the cryotomograms, but the gap between the filament bundle and the membrane appears  
406 more similar to the cytoplasmic background than a region packed tightly with protein. Also, statistical  
407 analysis of 20x20x100 voxel subvolumes from within the gap showed only a 10% increase in the mean  
408 pixel value compared to cytoplasm in the same tomogram. Another possibility is that nodes are not so well-  
409 ordered, nor stable during constriction and they become more “fluid”, repeatedly breaking apart and  
410 reassembling under competing forces from Myo2p motors connected to the node and the AMR. This kind  
411 of instability would make for a very heterogeneous and disordered protein distribution in the gap, which  
412 would be consistent with the density seen in the tomograms.

413

414 Another possibility is that the distribution of protein mass within the nodes is significantly different than  
415 the model presented by Laplante et al., and the bulk of the protein is, for instance, distributed more evenly  
416 along the surface of the membrane, making it difficult to detect by ECT. In this case, it would be feasible  
417 to think the filament bundle is tethered to the membrane along its length by protein linkers that are simply  
418 too thin to be resolved in a cryotomogram, which typically attain 3-4 nm resolution (7). This linker would  
419 need to be at least ~27 nm long to connect the bundles in the AMR to the membrane directly, because that  
420 is the average nearest distance between the membrane and the closest filament in each of the 22 tomograms  
421 analyzed (SI Appendix/Fig. S7). Again, the most viable candidate that meets these requirements is Myo2p,  
422 which was suggested by fluorescence microscopy studies of ring assembly to exist as a unipolar myosin  
423 (14, 30), and aptly, its coiled-coil tail would have been difficult to resolve in our tomograms. Interestingly,  
424 Myo2p is essential for cytokinesis in *S. pombe* (31, 32), even in mutant strains where the motor activity of  
425 Myo2p has been greatly reduced (33), suggesting that it plays a critical role in some other function, such as  
426 linking the AMR to the membrane.

427  
428 The node protein formin Cdc12p nucleates and elongates unbranched F-actin from its plus-end (34). Much  
429 of the actin in the ring is Cdc12p-derived (35, 36), so it has been proposed that actin filaments might  
430 remain engaged with node-bound Cdc12p at their plus ends, thus connecting filaments to the membrane  
431 (14, 30). This arrangement is logically satisfying, because myosin II walks preferentially toward the actin  
432 plus-end, meaning that any myosin II motor bound to the filament would be putting tension on the  
433 membrane. Our tomographic data does not support a model where most filament ends are engaged with  
434 node-bound Cdc12, because given that there are 2-4 Cdc12 dimers per node (35, 37), 20-60% of filament  
435 plus-ends (half the total ends observed) would not be bound to Cdc12p. Super-resolution fluorescence  
436 localization data showed that Cdc12p exists in nodes ~45 nm away from the membrane (14), but the broad  
437 peak of filament-end to membrane distances observed by ECT (Fig. 7B) shows that the filament ends to the  
438 left of the peak do not cluster at 45 nm. If the majority of filament ends were bound to Cdc12p, one would

439 expect to see a peak around this distance. For now, exactly how the ring is bound to the membrane remains

440 unclear.

441

442

443

444

445

446

## 447 **Experimental Methods**

448

### 449 **Cell Synchronization, fluorescence imaging, and latrunculin A treatment**

450 To maximize the probability of cryosectioning/FIB milling through actively constricting division septa, a  
451 temperature sensitive mutant of *S. pombe* (*cdc25-22 rlc1-3GFP*) carrying a GFP-tagged regulatory light  
452 chain of myosin II was used. First, colonies grown on YES-agar plates at the permissive temperature (22°  
453 C) were harvested with a sterile loop and suspended in liquid YES media to an  $OD_{600} \sim 0.1$  and further  
454 grown at the permissive temperature with 180 rpm shaking. The cells were grown for ~24 hours and kept  
455 between  $OD_{600} = 0.1-0.5$ . The synchronization process was initiated at  $OD_{600} = 0.25$  with transfer to the  
456 restrictive temperature (36° C) for 3.5–4 hours with shaking. Once the OD doubled to 0.5 cells were  
457 inspected by light microscopy to ensure that most cells had more than doubled in length due to stalled entry  
458 into mitosis. At this point, the cells were shifted to the permissive temperature (22° C) and allowed to enter  
459 mitosis.

460

461 To prepare samples for ECT, around 45 min after the cells entered mitosis they were screened by  
462 epifluorescence microscopy on a Nikon Eclipse 90i microscope using a 100x oil objective (NA = 1.4) and a  
463 Photometrics CoolSnap HQ2 CCD for the early formation of rings at the mid-cell. Cells were monitored  
464 every 5–10 minutes until ~90% of cells contained intact rings that had begun to contract. Finally, ~5 ml of  
465 synchronized culture was either pelleted at 4° C and placed on ice for high pressure freezing (HPF) or un-  
466 pelleted cells were directly plunge-frozen on EM grids.

467

468 To disrupt F-actin within dividing cells the same synchronization process was used, but during ring  
469 constriction latrunculin A (LatA, molecular probes #L12370) was added to the culture to a final  
470 concentration of 10  $\mu$ M. Within 10 min the continuous fluorescent ring became fragmented into puncta  
471 along the membrane around the mid-cell. Cells were then pelleted for HPF as described above.

472

### 473 **Characterization of cytokinesis in the temperature-sensitive *Cdc25* mutant**

474 To ensure phenotypically normal cytokinesis in the temperature-sensitive *cdc25-22 S. pombe* mutant, we  
475 synchronized cells expressing a GFP-tagged regulatory light chain of myosin (Rlc1-3GFP) and an  
476 mCherry-tagged spindle pole protein (mCherry-Pcp1p) at the G2-M boundary. Transient inactivation of  
477 mitotic inducer phosphatase Cdc25p is a commonly employed approach for synchronization (6, 8, 9). After  
478 release to permissive temperature, elongated *cdc25-22* cells undergo phenotypically normal cytokinesis (SI  
479 [Appendix/Fig. S1](#)). Rlc1 formed a uniform ring like that of the wild-type cells (SI [Appendix/Fig. S1A](#)).  
480 Ring assembly and ring constriction started at the onset and the end of spindle pole body (SPB) separation  
481 (SI [Appendix/Fig. S1B](#)) respectively, similar to what occurs in wild-type cells (38). Though we did observe  
482 a modest delay in AMR formation (SI [Appendix/Fig. S1C](#)), the time taken for completion of cytokinesis  
483 was comparable to those of wild-type cells (SI [Appendix/Fig. S1D](#)). Importantly, our method of  
484 synchronization had no significant impact on the velocity of ring constriction (SI [Appendix/Fig. S1E & F](#)).  
485 Thus, synchronization by reversible heat inactivation of mitotic inducer Cdc25p does not significantly alter  
486 the dynamics of AMRs.

487

488 To characterize cytokinesis in *cdc25-22 rlc1-3GFP*, mid-log phase cells were spotted on a 2% Agar pad  
489 supplemented with YES media and observed under a custom built spinning disk confocal with an inverted  
490 Olympus IX-83,100X/1.4 plan-apo objective, a deep cooled Hamamatsu ORCA II-ER CCD camera and  
491 Yokogawa CSU:X1 spinning disk (Perkin-Elmer). A stack of 18–20 Z slices of 0.3 mm Z-step-size was  
492 collected every 2 min for an hour at 25° C using the Velocity software (Perkin-Elmer). Images were then  
493 rotated and cropped using the imageJ software to align cells and 3D reconstruction was done using the  
494 Velocity software.

495

496

## 497 **Cryosectioning and Cryo-FIB milling**

498 For cryosectioning, synchronized and LatA-treated *S. pombe cdc25-22 rlc1-3GFP* cells ( $OD_{600} = 0.5$ ) were  
499 harvested ( $7197 \times g$ , 10 min), and the pellet was mixed with 40% dextran (w/v) in YES media. The samples  
500 were transferred to brass planchettes and rapidly frozen in a HPM010 high-pressure freezing machine (Bal-  
501 Tec, Leica). Note that, the step of first transferring cells to the location of the high-pressure freezer, then  
502 mixing cells with dextran, and finally loading a high pressure planchette took  $\sim 10$ – $20$  min. During this  
503 period cells were kept on ice to slow down constriction and after cryopreservation was completed, unused  
504 cells on ice were imaged again to ensure that continuous fluorescent rings were still visible. (We found that  
505 precooling cells for 20 min on ice did not affect the ring's constriction rate measured by fluorescence  
506 microscopy and the characteristics of the actin bundle revealed by ECT). Cryosectioning of the vitrified  
507 samples was done as previously described (39, 40). Semi-thick (150–200 nm) cryosections were cut at  
508  $-145^{\circ}\text{C}$  or  $-160^{\circ}\text{C}$  with a  $25^{\circ}$  Cryodiamond knife (Diatome, Biel, Switzerland), transferred to grids  
509 (continuous carbon-coated 200-mesh copper) and stored in liquid nitrogen.

510

511 For cryo-FIB milling,  $4 \mu\text{l}$  of synchronized *cdc25-22 rlc1-3GFP* cells ( $OD_{600} = 0.5$ ) were applied to the  
512 carbon surface of a freshly glow-discharged copper Quantifoil R2/2 EM grid. Grids were then blotted  
513 manually, from the back, within the humidifying chamber (95%) of an FEI Mark IV Vitrobot by setting the  
514 blot number to zero and using a large pair of forceps to insert a piece of Whatman #1 filter paper through  
515 the open side port.

516

517 Plunge-frozen grids were then mounted in custom-modified Polara cartridges with channels milled through  
518 the bottom, which allowed samples to be milled at a low angle of incidence ( $\sim 10$ – $12^{\circ}$ ) with respect to the  
519 carbon surface. These modified cartridges were transferred into an FEI Versa 3D equipped with a Quorum  
520 PP3010T Cryo-FIB/SEM preparation system. Samples were sputter coated with 20 nm of platinum prior to  
521 milling to minimize curtaining and to protect the front edge of the sample during milling. Vitrified cells

522 lying approximately perpendicular to the FIB beam were located and lamellae (~12  $\mu\text{m}$  wide and ~2  $\mu\text{m}$   
523 thick) were rough-milled at the mid-cell with beam settings of 30 keV and 0.300 nA. A polishing mill at a  
524 reduced current of 30 pA was then performed to bring the final thickness to 150–400 nm. Samples were  
525 then removed from the scope while maintaining a temperature below  $-160^{\circ}\text{C}$  and stored in liquid nitrogen.

526

### 527 **Cryo-fluorescence light microscopy (Cryo-FLM)**

528 Frozen grids with attached cryosections were loaded into Polara EM cartridges, transferred into a cryo-  
529 FLM stage (FEI Cryostage described in Nickell et al., 2006, modified to hold Polara EM cartridges as  
530 described in (41)) and imaged on a Nikon Eclipse Ti inverted microscope using a 60 $\times$  extra-long-working-  
531 distance air objective (Nikon CFI S Plan Fluor ELWD 60 $\times$  NA 0.7 WD 2.62-1.8 mm) and an Andor CCD.  
532 Focal stacks of each grid square covered by cryosectioned material were collected using the GFP filter set.  
533 Pairs of fluorescent puncta (corresponding to the two sides of the septum) were located within the  
534 cryosections and targeted for ECT after transfer to an FEI Tecnai F30 Polara TEM. Fluorescence images  
535 were scaled to the electron micrographs, and then overlaid and registered using the whole-cell background  
536 fluorescence from the cryosectioned cells.

537

### 538 **Electron cryotomography (ECT) and image processing**

539 Tilt-series of division septa in both cryosections and cryo-FIB milled lamellae were collected on an FEI  
540 Tecnai F30 Polara TEM operating at 300 keV every one degree from  $-60^{\circ}$  to  $+60^{\circ}$  with a total dose of 140–  
541 180 electrons/ $\text{\AA}^2$ . 4k x 4x images were collected with a Gatan K2 Summit direct electron detector in  
542 counting mode. Tilt-series were binned to pixel sizes of 1.2 and 0.9 nm/px depending on their original  
543 magnification, and then reconstructed using the patch tracking method included in the IMOD image  
544 processing suite (42).

545

546 Actin centerlines were computationally extracted using a template matching/tracing algorithm implemented  
547 within the Amira image segmentation software (43). Before filament extraction, tomograms were denoised  
548 using Nonlinear Anisotropic Diffusion filtering in IMOD. To segment the actin filaments, a 3.5 nm radius  
549 surface was generated around the filament centerline to match the actual size of actin filaments. Division  
550 septum membranes in each tomogram were hand segmented in Amira. Histograms of nearest distance  
551 measurements between segmented filament surfaces and the septum membrane were generated by surface-  
552 to-surface measurements within Amira. Nearest neighbor distances between filaments were calculated from  
553 the coordinates of the extracted filament centerlines using a custom script.

554

### 555 **Actin Straightness**

556 For each filament we calculated its contour length  $L_{contour}$  (as traced by the actin-segmentation software  
557 described above) and the length of a straight line connecting the two ends  $L_{end-to-end}$ . Filament  
558 straightness was then defined as the ratio  $L_{end-to-end}/L_{contour}$ .

559

### 560 **Calculation of persistence length**

561 Theoretically, the tangent correlation  $\langle \cos\theta \rangle$ , where  $\theta$  is the angle between the tangent vector at position 0  
562 and the tangent vector at a distance  $L$  along the filament, is defined as

$$\langle \cos\theta \rangle = e^{-L/L_p}$$

563 where  $L_p$  is the filament's persistence length. This formula can be expressed as

$$\log\langle \cos\theta \rangle = -L/L_p$$

564 To calculate the persistence length of the segmented filaments, each filament was modeled as a chain of  
565 beads with adjacent beads separated by 5 nm. Tangent correlation  $\langle \cos\theta \rangle$  was then calculated along the  
566 beads and  $\log\langle \cos\theta \rangle$  was plotted vs  $L$  to derive the persistence length  $L_p$ . See [SI Appendix/Fig. S8A](#).

567

568

## 569 **Calculation of ring diameter**

570 The average diameter of our synchronized cells (4.5  $\mu\text{m}$ , SD = 0.18  $\mu\text{m}$ , N = 30) was measured from DIC  
571 images collected on a Nikon Eclipse 90i microscope using a 100x oil objective (NA = 1.4) and a  
572 Photometrics CoolSnap HQ2 CCD with a detector pixel size of 6.5  $\mu\text{m}$ . For simplicity, the cell diameter  
573 was assumed to be 4.5  $\mu\text{m}$  for all cells imaged by ECT. By measuring the width of cell section  $A = 2a$  (SI  
574 [Appendix/Fig. S9](#)) we could calculate the distance  $c$  from the center to the section using the Pythagorean  
575 theorem as following

$$c^2 = r_{cell}^2 - a^2$$

576 where  $r_{cell}$  was the radius of the cell.

577 Next, by measuring the distance  $B = 2b$  between the two septal tips in the section we could calculate the  
578 ring radius using the Pythagorean theorem:

$$r_{ring}^2 = b^2 + c^2 = r_{cell}^2 - a^2 + b^2$$

579

## 580 **Average filament length and number of filaments per ring**

581 To calculate the average filament length we assume each tomogram was representative of the ring such that  
582 the filaments were uniformly distributed around the ring. As a result, the ratio of filament length to the  
583 number of ends was constant and equaled  $L_a/2$  for each filament of average length  $L_a$  had two ends. By  
584 calculating the total filament length  $L_{sum}$  and total number of ends  $N_e$  in the tomogram we derived the  
585 average length as:

$$L_a = 2L_{sum}/N_e$$

586 To calculate the total number of filaments in the ring  $N_{fil}$  we calculated the density of filament ends in the  
587 tomogram as  $N_e/T$  where  $T$  was the tomogram thickness. As this density was assumed to be uniform, it  
588 was theoretically equal to the ratio of the total number of ends in the ring  $2N_{fil}$  to the ring length  $\pi D_{ring}$ , or

$$\frac{N_e}{T} = \frac{2N_{fil}}{\pi D_{ring}}$$

589 The total number of filaments in the ring was then calculated as:

$$N_{fil} = \frac{\pi D_{ring} N_e}{2T}$$

590

591 **Acknowledgments**

592 The authors thank Catherine Oikonomou for revising the manuscript for clarity and Frances Allen for initial  
593 training and guidance in cryo-FIB milling.

594 M.M. is an Intermediate Fellow of the Wellcome Trust-DBT India Alliance (IA/I/14/1/501317). M.M.  
595 acknowledges the India Alliance and the DAE/TIFR for funds.

596

## 597 **References**

- 598 1. Schroeder TE (1973) Actin in dividing cells: contractile ring filaments bind heavy meromyosin.  
599 *Proc Natl Acad Sci USA* 70(6):1688–1692.
- 600 2. Mabuchi I, Okuno M (1977) The effect of myosin antibody on the division of starfish blastomeres. *J*  
601 *Cell Biol* 74(1):251–263.
- 602 3. Balasubramanian MK, Bi E, Glotzer M (2004) Comparative analysis of cytokinesis in budding yeast,  
603 fission yeast and animal cells. *Curr Biol* 14(18):R806–18.
- 604 4. Cheffings TH, Burroughs NJ, Balasubramanian MK (2016) Actomyosin Ring Formation and  
605 Tension Generation in Eukaryotic Cytokinesis. *Curr Biol* 26(15):R719–R737.
- 606 5. Kanbe T, Kobayashi I, Tanaka K (1989) Dynamics of cytoplasmic organelles in the cell cycle of the  
607 fission yeast *Schizosaccharomyces pombe*: three-dimensional reconstruction from serial sections. *J*  
608 *Cell Sci* 94 ( Pt 4):647–656.
- 609 6. Kamasaki T, Osumi M, Mabuchi I (2007) Three-dimensional arrangement of F-actin in the  
610 contractile ring of fission yeast. *J Cell Biol* 178(5):765–771.
- 611 7. Gan L, Jensen GJ (2012) Electron tomography of cells. *Q Rev Biophys* 45(1):27–56.
- 612 8. Nurse P (1975) Genetic control of cell size at cell division in yeast. *Nature* 256(5518):547–551.
- 613 9. Russell P, Nurse P (1986) *cdc25+* functions as an inducer in the mitotic control of fission yeast. *Cell*  
614 45(1):145–153.
- 615 10. Rigort A, et al. (2012) Automated segmentation of electron tomograms for a quantitative description  
616 of actin filament networks. *J Struct Biol* 177(1):135–144.
- 617 11. Courtemanche N, Pollard TD, Chen Q (2016) Avoiding artefacts when counting polymerized actin  
618 in live cells with LifeAct fused to fluorescent proteins. *Nat Cell Biol* 18(6):676–683.
- 619 12. Burgoyne T, Muhamad F, Luther PK (2008) Visualization of cardiac muscle thin filaments and  
620 measurement of their lengths by electron tomography. *Cardiovasc Res* 77(4):707–712.
- 621 13. Isambert H, et al. (1995) Flexibility of actin filaments derived from thermal fluctuations. Effect of  
622 bound nucleotide, phalloidin, and muscle regulatory proteins. *J Biol Chem* 270(19):11437–11444.
- 623 14. Laplante C, Huang F, Tebbs IR, Bewersdorf J, Pollard TD (2016) Molecular organization of  
624 cytokinesis nodes and contractile rings by super-resolution fluorescence microscopy of live fission  
625 yeast. *Proceedings of the National Academy of Sciences* 113(40):E5876–E5885.
- 626 15. Cooper JA (1987) Effects of cytochalasin and phalloidin on actin. *J Cell Biol* 105(4):1473–1478.
- 627 16. Schroeder TE (1972) The contractile ring. II. Determining its brief existence, volumetric changes,  
628 and vital role in cleaving *Arbacia* eggs. *J Cell Biol* 53(2):419–434.
- 629 17. Maupin P, Pollard TD (1986) Arrangement of actin filaments and myosin-like filaments in the  
630 contractile ring and of actin-like filaments in the mitotic spindle of dividing HeLa cells. *J Ultrastruct*  
631 *Mol Struct Res* 94(1):92–103.

- 632 18. Mabuchi I, Tsukita S, Tsukita S, Sawai T (1988) Cleavage furrow isolated from newt eggs:  
633 contraction, organization of the actin filaments, and protein components of the furrow. *Proc Natl*  
634 *Acad Sci USA* 85(16):5966–5970.
- 635 19. Pollard TD, Wu J-Q (2010) Understanding cytokinesis: lessons from fission yeast. *Nat Rev Mol Cell*  
636 *Biol* 11(2):149–155.
- 637 20. Proctor SA, Minc N, Boudaoud A, Chang F (2012) Contributions of turgor pressure, the contractile  
638 ring, and septum assembly to forces in cytokinesis in fission yeast. *Curr Biol* 22(17):1601–1608.
- 639 21. Pollard TD, Cooper JA (2009) Actin, a Central Player in Cell Shape and Movement. *Science*  
640 326(5957):1208–1212.
- 641 22. Fishkind DJ, Wang YL (1993) Orientation and three-dimensional organization of actin filaments in  
642 dividing cultured cells. *J Cell Biol* 123(4):837–848.
- 643 23. Al-Khayat HA (2013) Three-dimensional structure of the human myosin thick filament: clinical  
644 implications. *Glob Cardiol Sci Pract* 2013(3):280–302.
- 645 24. Trus BL, et al. (1989) Interactions between actin and myosin filaments in skeletal muscle visualized  
646 in frozen-hydrated thin sections. *Biophys J* 55(4):713–724.
- 647 25. Pollard TD (1982) Structure and polymerization of *Acanthamoeba* myosin-II filaments. *J Cell Biol*  
648 95(3):816–825.
- 649 26. Sinard JH, Stafford WF, Pollard TD (1989) The mechanism of assembly of *Acanthamoeba* myosin-  
650 II minifilaments: minifilaments assemble by three successive dimerization steps. *J Cell Biol* 109(4 Pt  
651 1):1537–1547.
- 652 27. Wu JQ, Bähler J, Pringle JR (2001) Roles of a Fimbrin and an  $\alpha$ -Actinin-like Protein in Fission Yeast  
653 Cell Polarization and Cytokinesis. *Mol Biol Cell* 12(4):1061–1077.
- 654 28. Wu J-Q, et al. (2006) Assembly of the cytokinetic contractile ring from a broad band of nodes in  
655 fission yeast. *J Cell Biol* 174(3):391–402.
- 656 29. Vavylonis D, Wu J-Q, Hao S, O'Shaughnessy B, Pollard TD (2008) Assembly mechanism of the  
657 contractile ring for cytokinesis by fission yeast. *Science* 319(5859):97–100.
- 658 30. Laporte D, Coffman VC, Lee I-J, Wu J-Q (2011) Assembly and architecture of precursor nodes  
659 during fission yeast cytokinesis. *J Cell Biol* 192(6):1005–1021.
- 660 31. Kitayama C, Sugimoto A, Yamamoto M (1997) Type II myosin heavy chain encoded by the *myo2*  
661 gene composes the contractile ring during cytokinesis in *Schizosaccharomyces pombe*. *J Cell Biol*  
662 137(6):1309–1319.
- 663 32. May KM, Watts FZ, Jones N, Hyams JS (1997) Type II myosin involved in cytokinesis in the fission  
664 yeast, *Schizosaccharomyces pombe*. *Cell Motil Cytoskeleton* 38(4):385–396.
- 665 33. Laplante C, et al. (2015) Three myosins contribute uniquely to the assembly and constriction of the  
666 fission yeast cytokinetic contractile ring. *Curr Biol* 25(15):1955–1965.
- 667 34. Kovar DR, Kuhn JR, Tichy AL, Pollard TD (2003) The fission yeast cytokinesis formin Cdc12p is a  
668 barbed end actin filament capping protein gated by profilin. *J Cell Biol* 161(5):875–887.

- 669 35. Coffman VC, Nile AH, Lee I-J, Liu H, Wu J-Q (2009) Roles of formin nodes and myosin motor  
670 activity in Mid1p-dependent contractile-ring assembly during fission yeast cytokinesis. *Mol Biol*  
671 *Cell* 20(24):5195–5210.
- 672 36. Coffman VC, Sees JA, Kovar DR, Wu J-Q (2013) The formins Cdc12 and For3 cooperate during  
673 contractile ring assembly in cytokinesis. *J Cell Biol* 203(1):101–114.
- 674 37. Wu J-Q, Pollard TD (2005) Counting cytokinesis proteins globally and locally in fission yeast.  
675 *Science* 310(5746):310–314.
- 676 38. Wu J-Q, Kuhn JR, Kovar DR, Pollard TD (2003) Spatial and temporal pathway for assembly and  
677 constriction of the contractile ring in fission yeast cytokinesis. *Dev Cell* 5(5):723–734.
- 678 39. Ladinsky MS, Pierson JM, McIntosh JR (2006) Vitreous cryo-sectioning of cells facilitated by a  
679 micromanipulator. *J Microsc* 224(Pt 2):129–134.
- 680 40. Ladinsky MS (2010) Micromanipulator-assisted vitreous cryosectioning and sample preparation by  
681 high-pressure freezing. *Meth Enzymol* 481:165–194.
- 682 41. Briegel A, et al. (2010) Correlated light and electron cryo-microscopy. *Meth Enzymol* 481:317–341.
- 683 42. Kremer JR, Mastrorarde DN, McIntosh JR (1996) Computer visualization of three-dimensional  
684 image data using IMOD. *J Struct Biol* 116(1):71–76.
- 685 43. Rigort A, et al. (2012) Automated segmentation of electron tomograms for a quantitative description  
686 of actin filament networks. *J Struct Biol* 177(1):135–144.
- 687